

1            Milikelvin-precision temperature sensing for advanced  
2            cryogenic detectors

3            M. Antonova<sup>a</sup>, J. Capó<sup>a</sup>, A. Cervera<sup>a</sup>, P. Fernández<sup>a,2</sup>, M. Á. García-Peris<sup>a,1,\*</sup>, X.  
4            Pons<sup>b</sup>

<sup>a</sup>*Instituto de Fisica Corpuscular Catedratico Jose Beltran 2 E-46980 Paterna (Valencia) Spain*

<sup>b</sup>*CERN Espl. des Particules 1 1211 Meyrin Switzerland*

---

5            **Abstract**

Precise temperature monitoring —to the level of a few milli-Kelvin— is crucial for the operation of large-scale cryostats requiring a recirculation and purification system. In particular, the performance of Liquid Argon Time Projection Chambers —such as those planned for DUNE— heavily relies on proper argon purification and mixing, which can be characterized by a sufficiently dense grid of high-precision temperature probes. In this article, a novel technique for the cross-calibration of Resistance Temperature Detectors (RTDs) in cryogenic liquids (argon and nitrogen) is presented, obtaining an unprecedented precision of 2.5 mK.

6            *Keywords:* Detectors, Liquid Argon, Cryogenics, Temperature, RTD, Purity,  
7            Computational Fluid Dynamics

---

8            **1. Introduction**

9            Precise temperature sensing is essential in large cryogenic detectors, where the circulation  
10          and purification of cryogenic liquids can have a major impact on overall detector perfor-  
11          mance. In these systems, uncontrolled temperature differences can modify the cryostat  
12          dynamics, ultimately affecting the physics sensitivity of the experiment. In this work, we  
13          present the calibration procedure of a novel temperature monitoring system developed  
14          for a prototype of the future DUNE experiment.

---

\*Corresponding author

Email address: [miguel.garcia-peris@manchester.ac.uk](mailto:miguel.garcia-peris@manchester.ac.uk) (M. Á. García-Peris)

<sup>1</sup>now in the University of Manchester

<sup>2</sup>now at Donostia International Physics Center, DIPC

15 DUNE, which stands for Deep Underground Neutrino Experiment [2], is expected to  
16 begin taking data towards the end of the decade. It aims at performing comprehensive  
17 neutrino oscillation analyses,—broadly exploring the Charge-Parity violation parameters  
18 phase-space and resolving the neutrino-mass hierarchy problem [6]. Its vast physics pro-  
19 gram also includes searches for hypothetical proton decay channels [3], multi-messenger  
20 astronomy from supernovae and neutrino bursts [8], and explorations of Beyond the  
21 Standard Model (BSM) physics [7]. With the most powerful neutrino beam ever built,  
22 produced at Fermilab, the experiment follows the long-baseline neutrino oscillations ap-  
23 proach, with two detectors. The Near Detector, also at Fermilab, will characterize the  
24 unoscillated neutrino beam. The Far Detector (FD), located in the Sandford Under-  
25 ground Research Facility (SURF), 1300 away from the ND and 1.5 km underground, will  
26 measure the oscillated flux.

27 DUNE phase I far detector will have two Liquid Argon Time Projection Chambers  
28 (LArTPC), and is expected to operate by 2029. DUNE phase II will complement with two  
29 more modules by mid 30's, aiming at a total fiducial mass of 40 kilotonnes. The detector  
30 technology has been established, with excellent tracking and calorimetric capabilities,  
31 in several smaller-scale experiments [10, 13]. The first demonstration of the technology  
32 at the kilotonne scale has been carried out at the CERN Neutrino Platform as part of  
33 the ProtoDUNE program. In particular, the ProtoDUNE-SP experiment [1] reproduced  
34 the detector components of the second DUNE FD module [4] at a scale 1:1 with a total  
35 argon mass 20 times smaller (770 tonnes). It was operated from mid-2018 to mid-2020,  
36 constituting the largest monolithic LArTPC to be built and operated up to date [5, 9].

37 During ProtoDUNE-SP operation, the level of impurities was kept way below 100 ppt  
38 oxygen equivalent using a cryogenic recirculation and purification system [1, 9]. This is  
39 fundamental in a LArTPC, as the 3D images produced by charged particles traversing  
40 the detector can be exponentially attenuated by medium impurities such as nitrogen,  
41 oxygen and water, biasing the energy measurements by absorbing ionization electrons.  
42 Three purity monitors, based on the ICARUS design [25], were installed outside the  
43 active volume of the TPC to measure the electron lifetime, which is inversely related  
44 to the residual concentration of impurities. They ran twice a day to monitor the argon  
45 purity and thus to provide the necessary corrections for posterior data analysis.

Achieving the necessary argon purity has been possible thanks to the studies based on computational fluid dynamic (CFD) simulations, and the experience gained with previous LArTPC demonstrators such as LAPD [11] and the 35-tonne prototype [12, 18], which have paved the way to operate large-scale cryostats requiring low concentrations of impurities. These studies have also shown that it exists a strong correlation between temperature and purity in the liquid argon volume. The distribution of impurities is insensitive to small ( $\mathcal{O} \sim 1$  K) absolute temperature variations, but strongly depends on the relative vertical temperature gradient. As the bulk volume in the cryostats needs to be continuously mixed with the incoming purified argon to ensure the purification of the whole LAr volume, the temperature distribution acts as a clear indicator of that mixing: a homogeneous temperature distribution indicates that the liquid is being properly mixed, whereas large temperature gradients constitute a clear symptom of deficient mixing. If the LAr bulk volume is not mixed properly, a stratification regime can develop: a significant portion of the liquid remains unpurified, generating ‘dead’ regions inside the detector. Hence, a constant monitoring of this temperature gradient can identify and mitigate potential failures of the purification system. In ProtoDUNE-SP, this gradient was predicted to be about 15 mK by the CFD simulations [1, 4].

The CFD simulations also predict, in spite of homogeneous mixing, that the concentration of impurities may also vary across the cryostat volume, requiring a position-dependent electron lifetime correction. The Purity Monitors themselves are intrusive objects which cannot be deployed inside the active volume, rather in only a few well-defined locations near the cryostat walls; thus, precise inference of the electron lifetime map requires alternative methods, as the one proposed in this article. A net of temperature sensors cross-calibrated to the <5 mK level should allow the measurement of a 15 mK temperature gradient, which can be used to constraint CFD simulations, providing a data-driven prediction of the impurity concentration. The main limitations of this new approach are the precision of the cross-calibration of the temperature sensors and the accuracy of the simulations. In this article, precise temperature monitoring for ProtoDUNE-SP will be described with particular emphasis on sensor calibration.

75    **2. The temperature monitoring system of ProtoDUNE-SP**

76    ProtoDUNE-SP [1] was the single-phase (SP) demonstrator of DUNE far detector second  
77    module [4], currently known as Horizontal Drift (HD) module. The elements constitut-  
78    ing the TPC, its associated readout electronics and the photon detection system, were  
79    housed in a 8x8x8 m<sup>3</sup> cryostat that contained the LAr target material. The cryostat,  
80    a free-standing steel-framed vessel with an insulated double membrane, is based on the  
81    technology used for liquefied natural gas storage and transport. A cryogenic system main-  
82    tains the LAr at a stable temperature of about 87 K, and ensures the required purity  
83    level by means of a closed-loop process that recovers the evaporated argon, recondenses  
84    it, filters it, and returns it to the cryostat, keeping the LAr level at about 7.3 m from the  
85    bottom membrane. ProtoDUNE-SP was exposed to a charged particle test-beam from  
86    October to November 2018, and later recorded cosmic rays until January 2020 [5, 9]. It  
87    was finally emptied and decommissioned in Summer 2020.

88       In order to understand the LAr behaviour inside the cryostat and validate the CFD  
89    simulations, 92 high-precision temperature sensors were installed inside ProtoDUNE-  
90    SP, near the active volume. These sensors were distributed in two vertical arrays, or  
91    Temperature Gradient Monitors (TGM), and two horizontal grids below and above the  
92    TPC, respectively. Three elements were common to all systems: sensors, cables and  
93    readout electronics. RTD technology [22] was chosen for this application. It consists of a  
94    metallic element whose resistance changes with temperature. This resistance is measured  
95    by feeding the RTD with a known current and measuring the resulting voltage. Based  
96    on previous experience from other prototypes [12], Lake Shore PT102 platinum sensors  
97    [21] with 100 ohms resistance at room temperature were chosen. Sensors were mounted  
98    on a 52x14 mm<sup>2</sup> PCB with an IDC-4 connector, such that they could be plugged-in at  
99    any time. Several versions of the PCB have been explored, finally converging to the one  
100   shown in Fig. 1, which minimizes the contact of the sensor with the PCB while keeping  
101   the sensor protected.

102      A careful choice of the readout cable and the connections are essential to obtain the  
103    required temperature precision. See for example [22] for a detailed description. A custom  
104    cable made by Axon [14] was used. It consists of four American Wire Gauge (AWG) 28  
105   teflon-jacketed copper wires, forming two twisted pairs, with a metallic external shield

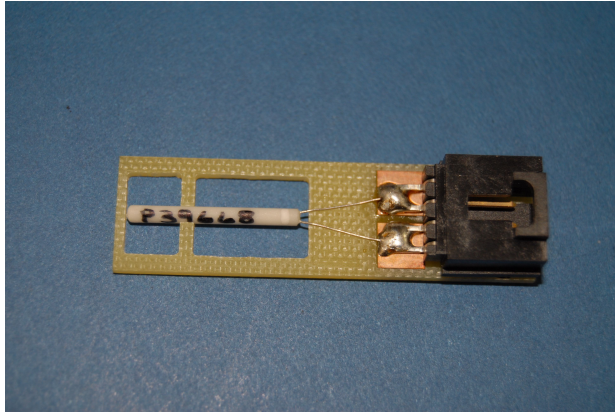


Figure 1: PCB support with temperature sensor and IDC-4 connector. The transition from two wires at the sensor to 4 wires at the readout is clearly seen. The sensor has a length of 2 cm.

and an outer teflon jacket. The outer diameter of the cable is 3.7 mm. Teflon was chosen for its good thermal properties and low out-gassing. The metallic external shield (connected to the readout in one end and left floating at the sensor's end) and the twisted pairs are crucial to reduce the effect of external electromagnetic noise pickup. When RTDs are far from the voltmeter, the resistance of cables and connectors are added to the one of the sensor, biasing the temperature measurement. This bias can be subtracted to some level, but cannot be fully controlled since the resistance of those elements also depends on temperature. To minimise the impact of this effect a four wire readout is introduced [22], such that the voltage is measured in the vicinity of the RTD.

The last common element is the readout system, consisting of a very precise 1 mA current source to excite the sensors and a 24 bits ADC to measure the voltage. The readout system will be described in detail in section 3.

As previously mentioned, ProtoDUNE-SP CFD simulations predict vertical temperature gradients as low as 15 mK [1]. A relative precision better than 5 mK was required to validate and tune those simulations with sufficient confidence. Three main ingredients are necessary to obtain such a precision: i) high quality and stable temperature probes, ii) a very precise readout system, and iii) a precise calibration, both for the readout and the sensors. As mentioned above, two TGMs were deployed in ProtoDUNE-SP: one could be moved vertically and hence calibrated *in situ*, while the other one —static—

125 fully relied on a prior calibration in the laboratory. In this article, the calibration of the  
126 static TGM [17] sensors is described in detail. This device consists of a vertical array  
127 of 48 sensors, installed 20 cm away from the lateral field cage.

128 The calibration was performed once in spring 2018 (a few months before the operation  
129 of ProtoDUNE-SP), and several times after ProtoDUNE-SP decommissioning. In this  
130 article the calibration setup, procedure and results will be described in detail. Compar-  
131 ison between the different calibration campaigns will be addressed, revealing important  
132 information about systematic uncertainties and RTD ageing.

133 **3. Readout system**

134 A precise and stable electronic readout system is needed to achieve the required precision.  
135 In previous versions of the calibration system, each sensor was connected to a different  
136 and independent electronic circuit and thus, fed by a different current and read by a  
137 different ADC channel. It was soon realized that the measured temperature difference  
138 between any two pairs of sensors was heavily affected by the electronic offset between  
139 channels. This offset was not constant, and showed dependence on ambient temperature  
140 and humidity, which affected both the current source and the ADC, generating variations  
141 of tens of mK for the measurement of a single calibration constant between sensors. A  
142 variant of an existing mass PT100 temperature readout system developed at CERN for  
143 one of the LHC experiments [16] was adapted to solve this problem. The system consists  
144 of an electronic circuit that includes:

- 145 • A precise and accurate 1 mA current source for the excitation of the temperature  
146 sensors based on an application of the Texas Instruments precise voltage reference  
147 REF102CU with a possibility to adjust  $\pm 10\text{nA}$  with Keithley 2001 multimeter  
148 [15, 23].
- 149 • A multiplexing circuit based on the Analog Devices ADG1407BRUZ multiplexer  
150 with ultralow internal resistance in an 8-channel differential configuration. The  
151 readout circuit contains three multiplexers, providing a readout capacity of 24  
152 channels. The multiplexing circuit and the current sourced are realised in a single  
153 card (see Fig. 2).

- 154     ● A readout system based on National Instruments Compact RIO-FPGA device [19]  
 155       equipped with a NI-9238 analogue input module that provide 24 bits of resolution  
 156       over 1 volt range [20]. By programming the Van Dusen equation the readout  
 157       calculates the temperature in Kelvin units. The Compact RIO also drives the  
 158       control bits of the multiplexers

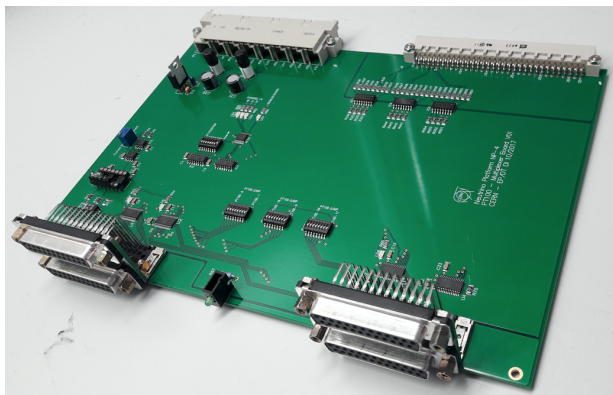


Figure 2: Current source and multiplexing card with 24 channels.

159 One of the features of the readout circuit is the serialization of the current source exci-  
 160 tation for all the sensors connected to the same board, such that the same 1 mA current  
 161 is delivered to all of them. Multiplexing the signal of the sensors such that they can be  
 162 readout by the same ADC channel minimises the residual offset due to the electronics.  
 163 This system was used during the calibration campaigns presented in this article and also  
 164 for the temperature measurements during ProtoDUNE-SP operation.

165 The readout was not considered a potential source of bias during the calibration  
 166 campaign prior to the installation in ProtoDUNE-SP (see Sec. 4) and it was not stud-  
 167 ied in detail at that time. However, aiming to improve the calibration results after  
 168 ProtoDUNE-SP operation, a more thoughtful study of the readout was performed before  
 169 the calibration campaigns presented in Sec. 5. In particular, the twelve channels (7-18)  
 170 used for sensor calibration were investigated. It was found that, despite the multiplexing  
 171 system, a small residual offset between channels still exists. Fig. 3 shows the offsets of  
 172 channels 8-18 with respect to channel 7, computed using twelve 20 ohms low Temperature

173 Coefficient of Resistance (TCR)<sup>3</sup> precision resistors, with an equivalent temperature of  
 174 76 K. Two of those, High Precision 1 (HP1) and High Precision 2 (HP2), are selected as  
 175 the measurement samples and connected to the reference channel (7) and the channel be-  
 176 ing calibrated (from 8-18), while leaving all other channels connected to other secondary  
 177 resistors to let the current flow through the system. The readout offset between chan-  
 178 nel 7 and channel X,  $\Delta T_{7-X}^{readout}$ , is then computed using the results of two consecutive  
 179 measurements:

- 180 1. HP1 in channel 7 and HP2 in the channel X being calibrated. The offset between  
 181 the measured temperatures is

$$\Delta T_{7-X}^A = T_X^{HP2} - T_7^{HP1} + \Delta T_{7-X}^{readout}. \quad (1)$$

- 182 2. HP2 channel 7 and HP1 in the channel X being calibrated. The offset between the  
 183 measured temperatures is

$$\Delta T_{X-7}^B = T_X^{HP1} - T_7^{HP2} + \Delta T_{7-X}^{readout}. \quad (2)$$

184 Because of the very low TCR of the resistors, it can be assumed that the resistances  
 185 are constants in those two measurements ( $T_7^{HP1} = T_X^{HP1}$  and  $T_7^{HP2} = T_X^{HP2}$ ). Thus,  
 186 the offset between channels 7 and X can be computed as the average between those two  
 187 measurements:

$$\Delta T_{7-X}^{readout} = \frac{\Delta T_{7-X}^A + \Delta T_{X-7}^B}{2}. \quad (3)$$

188 The results in Fig. 3, show an offset of up to 2.5 mK when comparing directly with  
 189 channel 7, while the offset between any other two channels is below 1 mK, indicating that  
 190 there is something special about the first channel being readout. Error bars in that figure  
 191 correspond to the standard deviation of four independent measurements (repeatability)  
 192 of the same offset (see Fig. 3). As it can be observed the error is below 0.5 mK, what  
 193 probes the great repeatability of the readout. These offsets are more likely due to parasitic

---

<sup>3</sup>The temperature coefficient of resistance is defined as the change in resistance per unit resistance per degree rise in temperature. Typically  $\pm 5\text{ppm}/^\circ\text{C}$ .

resistances in the different lines that are multiplexed. This finding allowed a correction to the measurements taken during the subsequent calibration campaigns, improving the obtained precision.

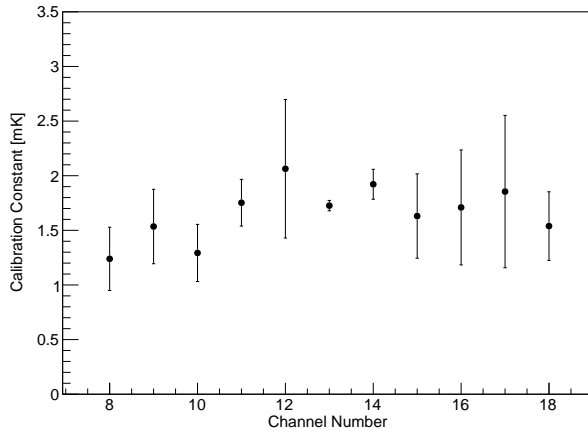


Figure 3: Offset between readout channels 8-18 and channel 7, used as reference. Points correspond to the mean of the 4 independent measurements and the error bars are their RMS.

#### 4. Calibration before the installation in ProtoDUNE-SP

The Lake Shore Cryotronics company provides PT102 RTDs with a temperature reading dispersion of about 0.1 K, which is insufficient for ProtoDUNE-SP's requirements. While the company offers additional calibration to the 10 mK level, the cost is prohibitive. R&D on sensor calibration was identified as a crucial ingredient for the success of the ProtoDUNE-SP temperature monitoring system. For this particular application, sensor calibration consists in finding the temperature offsets between any pair of sensors when exposing them to the same temperature. The experimental setup used for the calibration of RTDs before their installation in ProtoDUNE-SP had two main components: i) the readout system used to monitor the sensor's temperature (described in the previous section) and ii) the cryogenics vessel and the associated mechanical elements used to put sensors together under stable cryogenics conditions. They were developed to achieve a relative calibration with a precision better than 5 mK.

210    *4.1. Experimental setup*

211    The mechanics of the calibration setup evolved considerably since the initial tests until  
212    the final Static TGM calibration. Offset stability and repeatability drove this evolution.  
213    The final setup (see Fig. 4) consisted of the following elements:

- 214       • A polystyrene vessel formed by an outer box with dimensions  $35 \times 35 \times 30 \text{ cm}^3$  and  
215       4.5 cm thick walls, and a dedicated polystyrene cover, complemented by extruded  
216       polystyrene panels glued into the inner walls and floor of the outer box, to conform  
217       an inner empty volume of  $10 \times 10 \times 20 \text{ cm}^3$ .
- 218       • A  $10 \times 10 \times 20 \text{ cm}^3$  3D printed polylactic acid (PLA) box with two independent con-  
219       centric volumes, placed in the inner volume of the polystyrene vessel. Its purpose  
220       is twofold: i) to contain LAr, since polystyrene is porous to it, and ii) to create an  
221       smaller inner volume with further insulation and less convection.
- 222       • A cylindrical aluminum capsule, to be placed in the inner volume of the PLA box,  
223       with 5 cm diameter, 12 cm height and 1 mm thin walls. It had a circular aluminum  
224       cover with a small opening to extract the cables and to allow LAr to penetrate  
225       inside. The capsule was used to slowly bring sensors to cryogenic temperatures by  
226       partial immersion in LAr with no liquid inside, minimizing thermal stress. Alu-  
227       minum was chosen for its high thermal conductivity.
- 228       • A 3D printed PLA support for four sensors, to be placed inside the aluminum  
229       capsule, keeping sensors always in the same position with respect to each other and  
230       to the capsule walls.

231    The system described above provides stable conditions in the inner volume, with  
232    three levels of insulation: the outer polystyrene vessel and two PLA box LAr volumes.  
233    The aluminium capsule is key to this system and its usage constituted a turning point in  
234    the R&D since it minimises thermal shocks, which were identified as the main limiting  
235    factor for the repeatability of the sensor's offsets. Indeed, variations of several tenths  
236    of mK were observed in initial tests without the capsule. The problem was attributed  
237    to thermal shocks when, after many immersions in LN<sub>2</sub>, one of the sensors suffered a  
238    dramatic change in its offset (see Fig. 5). Examination at the microscope revealed cracks  
239    in the outer RTD ceramics (see Fig. 6).



Figure 4: Final calibration setup. Left: polystyrene box with PLA box and aluminum capsule. Middle: aluminum capsule. Right: Sensor's support with four sensors.

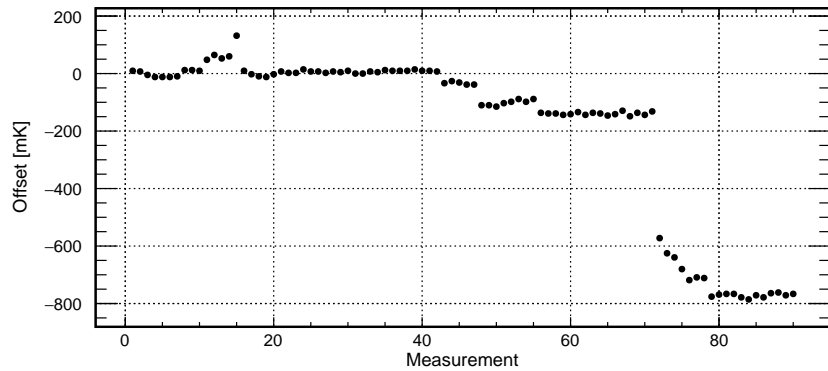


Figure 5: Offset between two sensors for 90 immersions in LN<sub>2</sub>. A drop of 800 mK is observed.

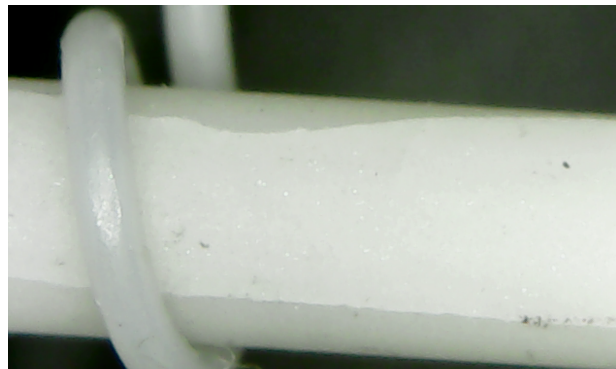


Figure 6: Cracks observed with the microscope in the ceramic of the sensor.

240    4.2. Calibration procedure

241    The calibration procedure relies on the assumption that all sensors in the capsule are at  
 242    the same temperature. This limits the number of RTDs in a single run to four, since  
 243    i) they should be as close as possible to each other and ii) as far as possible from the  
 244    capsule walls (the sensor closer to the wall could be biased). Two different methods,  
 245    described schematically in Fig. 7, were used to cross-calibrate all 48 sensors in runs of 4  
 246    sensors:

- 247    1. **Reference method:** all sensors are calibrated with respect to a reference one, in  
 248    sets of three sensors (the fourth one would be the reference sensor, which must be  
 249    present in all runs). In total there are sixteen calibration sets.
- 250    2. **Tree method:** Four different sets of sensors can be cross-calibrated by performing  
 251    a second round of measurements with a single promoted sensor from each of those  
 252    four sets. Since there are 16 sets in total, a third round of measurement is needed  
 253    to cross-calibrate the four sets in the second round.

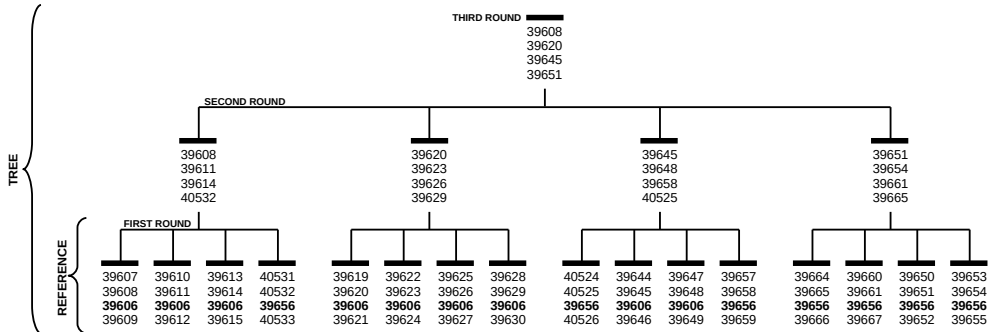


Figure 7: Schematic view of calibration sequence. Each number represents a different RTD, and the numbers in bold represent the reference sensors. The first round consists on a direct calibration respect to a reference sensor. The second and third rounds are needed to relate all sensors independently of the reference sensor.

254    The reference method was expected to be more precise since any two sensors were  
 255    related through a single intermediate sensor (the reference one), while for the tree method  
 256    the relation between any two sensors required more than one intermediate sensor. For  
 257    example, the offset between sensors  $i$  and  $j$  in different sets, related through sensors  $k$   
 258    and  $l$  in the second round, would be  $\Delta T_{ij} = \Delta T_{ik} + \Delta T_{kl} + \Delta T_{lj}$ . For sensors related

259 through the third round an additional term should be added, further increasing the offset  
260 uncertainty.

261 Offset repeatability is one of the key parameters to be understood since the laboratory  
262 calibration must be applicable to the real detector. This was studied by performing four  
263 independent calibration runs for each set of four sensors. However, because thermal  
264 fatigue of the reference sensor (64 thermal cycles for 4 repeatability runs) was a strong  
265 concern, three secondary reference sensors were used to regularly monitor the response  
266 of the primary reference sensor.

267 The following procedure is applied for each set of four sensors. First, they are placed  
268 inside the aluminium capsule. The sensor with the highest serial number is placed in the  
269 orange connector, and the one with the lowest in the red. The central connector closer to  
270 the red one is used for the reference sensor. These positions are easily called by numbers  
271 from 1 (orange) to 4 (red), as shown in Fig. 8-left.

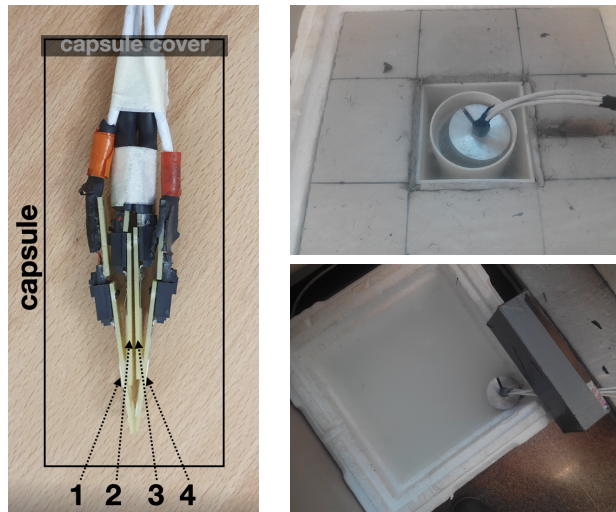


Figure 8: Left: Picture of sensor order inside the flask. Position 1 corresponds to highest serial number and 4 to lowest; position 3 is reserved to reference sensor. Top: Flask partially introduced in LAr. Bottom: Flask partially introduced in room water to warm up sensors before performing a new measurement.

272 After filling the PLA box with LAr, the aluminum capsule is partially immersed (see  
273 Fig. 8-right-top) such that the air inside cools-down slowly, avoiding direct exposure  
274 of the sensors to LAr, which would result in a thermal shock. When the monitored  
275 temperature approaches the one of LAr (< 95 K), which takes about 15 minutes, the

276 capsule is completely immersed, being filled with liquid. The PLA box is then completely  
277 filled with LAr to account for evaporation during the cool-down phase. Finally, the  
278 polystyrene vessel is closed using the polystyrene lid. The actual calibration runs for  
279 forty minutes.

280 When the measurement is finished, the capsule is extracted from the liquid, emptied  
281 of LAr and partially immersed into another polystyrene box filled with water at room  
282 temperature (see Fig. 8-right-bottom). The warm-up process takes about ten minutes.  
283 When sensors have reached a temperature around 250 K a new independent measurement  
284 can start.

285 Fig. 9 shows the typical evolution of the temperature for the four sensors in the capsule  
286 during the warm-up and cool-down processes. A sudden fall to 87 K is observed at about  
287 1950 seconds, which corresponds to total immersion of the sensors in LAr. Notice also  
288 that two of the sensors have lower temperature during the cool-down process; those are  
289 sensors 1 and 4, the ones closer to the capsule walls.

290 For each set of sensors the procedure described above is repeated four times, resulting  
291 in four independent measurements of the same offset. These measurements are used to  
292 compute a mean offset value and its standard deviation (repeatability from now on).

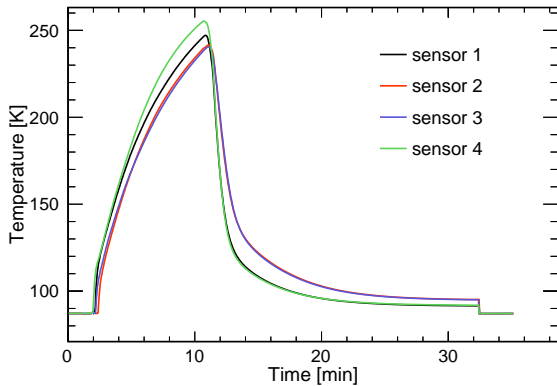


Figure 9: Temperature evolution during the warm-up and cool-down processes between two consecutive runs.

293 *4.3. Calibration results*

294 Here we present the results of the calibration using both calibration methods, a study of  
295 the consistency of these results, and a preliminary estimation of the systematic uncer-

296 tainty of the calibration process.

297 *4.3.1. Results on the first round of measurements*

298 Fig. 10 shows the offset of three different sensors with respect to the reference sensor as  
299 a function of time, and for four independent calibration runs. The offset is more stable  
300 for the sensor closer to the reference (position 2), while external sensors (positions 1  
301 and 4) have larger variations, but present similar patterns between them. This effect  
302 is attributed to the geometry of the system, with sensors at different heights and not  
303 symmetrically positioned with respect to the capsule walls, and was taken into account  
304 when developing the second version of the system, presented in Sec. 5.

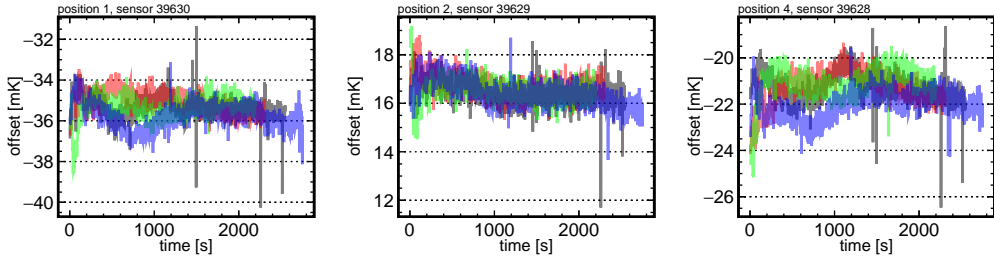


Figure 10: Offset between the reference sensor and each of the three sensors in a set, as a function of time. Each colour represents an independent measurement.

305 The mean offset for each sensor and each calibration run is computed as the average  
306 in the time range between 1000 and 2000 seconds, found to be the most stable region  
307 for most sensors. The standard deviation of the four measurements is taken as the  
308 uncertainty, also referred from now on as repeatability. As shown in Fig. 11, uncertainties  
309 are in general below 1 mK, demonstrating the great level of repeatability achieved.

310 *4.3.2. Time walk correction for reference sensors*

311 Time evolution of the response of sensor 39606 was studied by periodically (every  $\sim$ 20 im-  
312 mersions) computing its offset with respect to three secondary reference sensors, 39603,  
313 39604 and 39605. For each of those additional calibrations, two runs were taken in-  
314 stead of four in order to minimize thermal fatigue of the reference sensor. As shown  
315 in Fig. 12-left, the offset, computed as the mean of those two runs, varies linearly at a  
316 rate of 0.07 mK/immersion, which suddenly increases to 0.22 mK/immersion after 60  
317 runs. This change in the slope may be related with the frequency of immersions, which

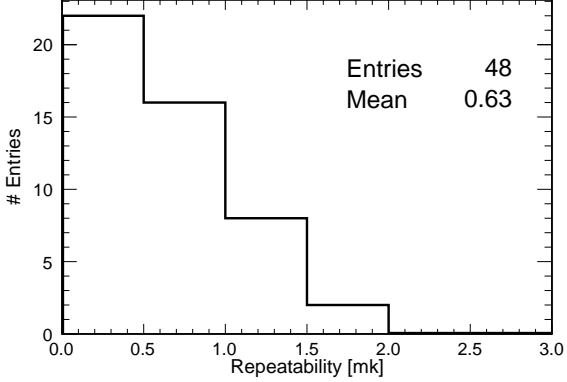


Figure 11: Distribution of the repeatability for calibration runs in the first round.

increased from 3/day to 5/day. Sensor 39606 was initially used for other purposes, and the calibration of the 48 sensors conforming the static TGM started approximately at immersion 40. Given this change in its response, sensor 39606 was substituted by 39656 as primary reference for the last quarter of the TGM calibration in order to avoid further fatigue and potential untraceable behaviour. The evolution of the new reference sensor is shown in Fig. 12-right. It is worth noting that the same slopes are valid for the three secondary reference sensors in both cases, supporting the idea that the change observed in the offsets can be exclusively attributed to thermal fatigue of the reference sensor.

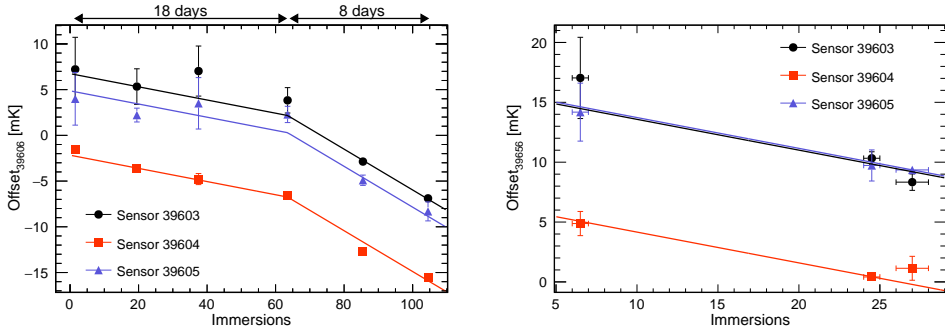


Figure 12: Offset between the reference sensors (39606 on the left panel and 39656 on the right panel) and the three secondary references as a function of the number of immersions. Offsets for sensor 39604 have smaller errors because of its position inside the capsule. Solid lines correspond to the parametrization in Eq. 4.

The zero intercept in both panels of Fig. 12 corresponds to the unbiased offset (or the

327 offset at  $N_{inmersion} = 0$ ) of each of the secondary reference sensors with respect to the  
 328 primary reference. In order to compute the unbiased offset for a sensor  $s$ , a time walk  
 329 correction after  $N$  immersions is calculated as

$$\Delta T_{s,06}(N=0) = \begin{cases} \Delta T_{s,06}(N) + (0.072 \pm 0.003) * N & N < 63.5 \\ \Delta T_{s,06}(N) + (0.072 \pm 0.003) * 63.5 + \\ \quad +(0.223 \pm 0.007) * (N - 63.5) & N > 63.5, \end{cases} \quad (4)$$

$$\Delta T_{s,56}(N=0) = \Delta T_{s,56}(N) + (0.168 \pm 0.007) * N. \quad (5)$$

330 All sensors can be related to the same primary reference sensor, 39606, adding the  
 331 unbiased offset between sensors 39606 and 39656,  $\Delta T_{56,06}(N=0)$ , to sensors calibrated  
 332 with respect to 39656. By averaging over the three secondary reference sensors, the value  
 333 obtained is  $\Delta T_{56,06}(N=0) = -9.19 \pm 0.13$  mK.

#### 334 4.3.3. Results on the reference method

335 Fig. 13 shows the offset of all sensors with respect to the 39606 reference. As it can  
 336 be noticed, the dispersion of the offsets is compatible with 0.1 K, the value quoted by  
 337 the vendor. Fig. 14-left shows the distribution of the repeatability of the computed  
 338 calibration constants after applying the different corrections, showing an average value  
 339 below 1 mK.

#### 340 4.3.4. Results on the tree method

341 The offsets are computed in this case with respect to an arbitrary reference among  
 342 all sensors being calibrated. Selecting as reference a sensor present in the third round  
 343 (see Fig. 7) minimises the number of operations to compute the offset, and hence the  
 344 uncertainty when computing the offset. Sensor 39645 was chosen as reference. Fig. 14-  
 345 right shows the distribution of the repeatability of the computed calibration constants,  
 346 the mean of which is slightly below the one obtained for the reference method. Thus,  
 347 it is confirmed that despite the higher number of intermediate sensors to relate any two  
 348 sensors, the additional uncertainty introduced by the time walk correction makes the  
 349 tree method superior to the reference method. Moreover, the reference method suffers a  
 350 —not yet known— systematic error associated to the time wall correction model.

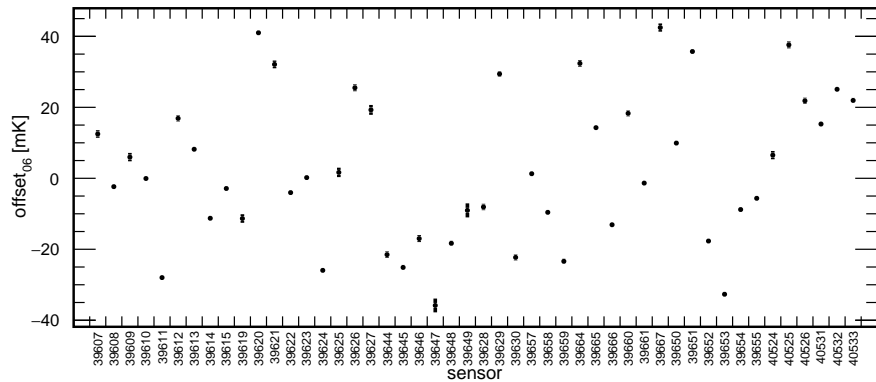


Figure 13: Offset of each sensor with respect to reference sensor 39606 using the reference method.

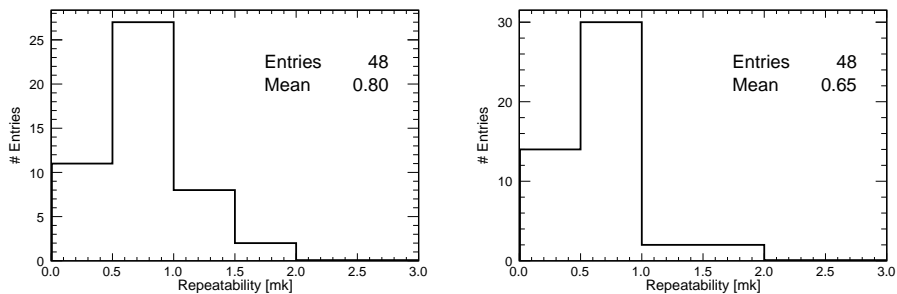


Figure 14: Left: repeatability distribution for the reference method. Right: repeatability distribution for tree method.

351    4.3.5. *Consistency cross-check and error estimation*

352    The uncertainties presented so far are in general below 1 mK, and they correspond to  
353    the standard deviation of the four independent measurements of each calibration con-  
354    stant plus the error propagation associated to the required corrections (time-walk for  
355    the reference method, addition of calibration constants for the tree method, and the  
356    uncorrected electronic residual offset for both). These corrections are likely to include  
357    unknown systematic effects in the final calibration constants. In order to estimate the  
358    overall final precision of the calibration, the following cross-check was performed. The  
359    calibration strategy provides two different calibration constants for each sensor, one for  
360    the reference method and another for the tree method. In the case of the sixteen sensors  
361    used in the second round of the calibration tree, these two values are statistically inde-  
362    pendent of each other, since they rely on different runs. Indeed, the reference method  
363    uses only the runs in the first round while the tree method for those sensors uses only  
364    runs in the second and third round. Thus, those 16 sensors can be used to estimate the  
365    precision of the calibration procedure by comparing the results of the two methods.

366    By construction, the result of subtracting the calibration constants obtained in the  
367    two methods should be compatible with the offset between sensors 39645 and 39606,  
368     $\Delta T_{45,06} = \Delta T_{s,06} - \Delta T_{s,45} = T_{45} - T_{06}$ , used as reference for the tree and reference  
369    methods respectively. This offset is found to be  $-25.1 \pm 0.7$  mK by direct measurement  
370    of the two sensors (see 10th column in Fig. 7). Fig. 15 shows this benchmark with (left)  
371    and without (right) time walk corrections for the 16 sensors aforementioned, probing  
372    the self-consistency of this correction. The standard deviation of this distribution, 2.4  
373    mK, is an estimation of the quadratic sum of the total uncertainty of both calibrations.  
374    Assuming that the reference sensor method has a larger uncertainty than the tree method  
375    due to the time walk correction, an upper limit of 1.7 mK for the total error of the tree  
376    method can be assumed. In the same way, this is the inferior limit for the total error of  
377    the reference method. In both cases, these errors are less than half of what was originally  
378    required for the TMS.

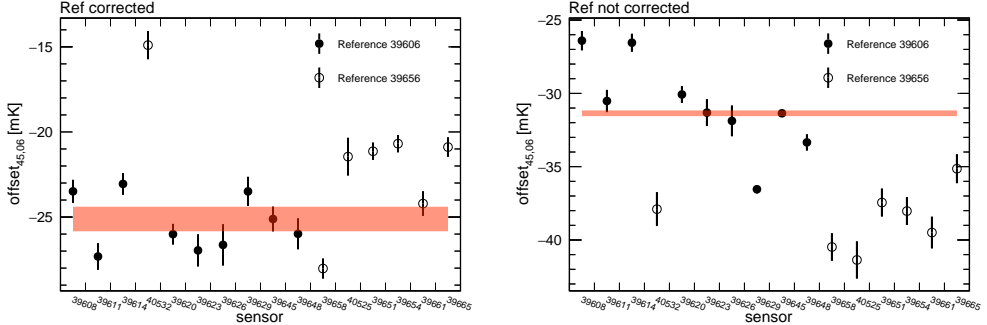


Figure 15:  $\Delta T_{45,06}$  computed through all sensors of the second stage of the calibration procedure. Left: applying corrections. Right: not applying corrections. A clear improvement is obtained using the corrections on the reference sensor. The red line represents the expected value of this calibration constant.

### 379 5. Re-calibration after ProtoDUNE-SP operation

380 After ProtoDUNE-SP decommissioning in 2020, temperature sensors were disconnected  
 381 from the TGM and re-calibrated several times (see Table 1), using both LAr and LN2 as  
 382 cryogenic liquid. The comparative analysis of those re-calibrations not only offers insights  
 383 into the long-term stability of the sensors but also elucidates any potential dependencies  
 384 on the choice of the cryogenic liquid. Although DUNE will use LAr, massive RTD  
 385 calibration would benefit from using LN2, given its higher accessibility and lower cost in  
 386 Spain.

date	cryogenic liquid	# sensors in capsule
March 2018	LAr	4
February 2022	LN2	14
March 2023	LN2	14
July 2023	LAr	14

Table 1: Calibration runs with indication of the date, the cryogenic liquid used and the number of sensors inside the capsule.

387 In this section, a description of the setup used for these new calibrations, the changes  
 388 applied to the procedure as well as the results and conclusions of these calibrations are  
 389 presented.

390    5.1. Evolution of the calibration setup

391    The Horizontal Drift far detector module will have more than 500 precision sensors [4],  
392    making the use of the calibration setup impractical for calibration purposes, since it  
393    can only accommodate four sensors simultaneously. Significant modifications have been  
394    introduced in order to increase this number to twelve, while maintaining the precision  
395    achieved during the 2018 calibration campaign. This was accomplished by positioning  
396    sensors at the same height, to avoid any potential vertical gradient, and following a  
397    cylindrical configuration, under the assumption that convection inside the capsule has  
398    rotational symmetry. This symmetry is also kept outside the capsule in all concentric  
399    cryogenic containers, having added a fourth independent volume which should further  
400    reduce convection inside the inner capsule. This notable advancement greatly streamlines  
401    the calibration process and serves to reduce both statistical and systematic errors asso-  
402    ciated with the procedure. Fig. 16 shows the different elements of the new calibration  
403    setup, which are described below:

- 404       • A polystyrene box with dimensions  $55 \times 35 \times 30 \text{ cm}^3$  and 4.5 cm thick walls with  
405       a dedicated cover of the same material.
- 406       • Extruded polystyrene rectangles with a cylindrical hole of 12.5 cm diameter and  
407       25 cm height, to conform the inner volume.
- 408       • A PTFE container with 12.5 cm diameter, 25 cm height and 2 mm thick walls to  
409       fit in the hole left in the box. The approximate volume is 2 L.
- 410       • A 3D printed PLA cylinder with two independent concentric volumes, placed inside  
411       the PTFE container.
- 412       • A cylindrical aluminum capsule to be placed in the inner volume of the PLA cylin-  
413       der. It has 7 cm diameter, 14 cm height and 1 mm thick walls.
- 414       • A 3D printed PLA holder for 14 sensors, 12 of them forming a circle (the ‘corona’)  
415       and the other 2 at the center, to be used as references. This support can be attached  
416       to the aluminum capsule at a fixed height. Cables are naturally extracted from the  
417       top of the assembly. A detailed view of this holder can be found in Fig. 16.

- 418     • The readout electronics, described in Sec. 3 has been retained from the previous  
 419     setup.  
 420     • A more cost effective cable with similar performance has been used. Produced by  
 421     Tempsens [24], it has four twisted cables instead of two separated twisted pairs  
 422     and an additional Kapton insulation layer between the shielding mesh and the four  
 423     conductors. Its diameter is 2.7 mm.

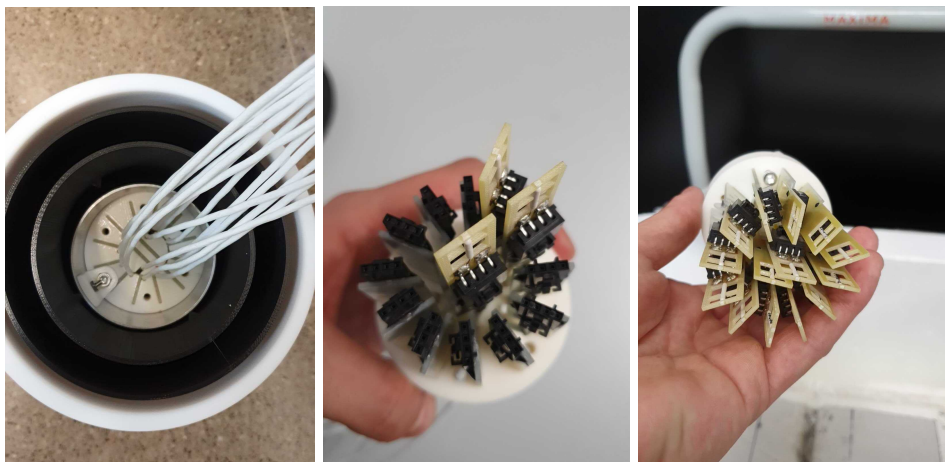


Figure 16: Left: The four concentric volumes. Center: A view of one of the references and two corona sensors. Right: The 12 corona sensors plus the 2 references.

424     *5.2. Calibration procedure*

425     The sensor support was originally designed to accommodate two reference sensors in  
 426     the center (see Fig. 16), enabling both the reference and tree calibration methods.  
 427     However, it was soon observed that temperature variations between corona and reference  
 428     sensors were significantly larger than those between any two corona sensors. This effect  
 429     is attributed to the convection pattern inside the capsule, which is expected to have  
 430     rotational invariance, and hence favour sensors disposed following a cylindrical symmetry.  
 431     This can be observed in Fig. 17-left, where the offset between two corona sensors is  
 432     nearly constant in time in four independent measurements, and in Fig. 17-right, where  
 433     the offset between a corona and a reference sensor shows a more chaotic behaviour.  
 434     Consequently, only the ‘tree’ calibration method was considered during the calibrations  
 435     after ProtoDUNE-SP decommissioning.

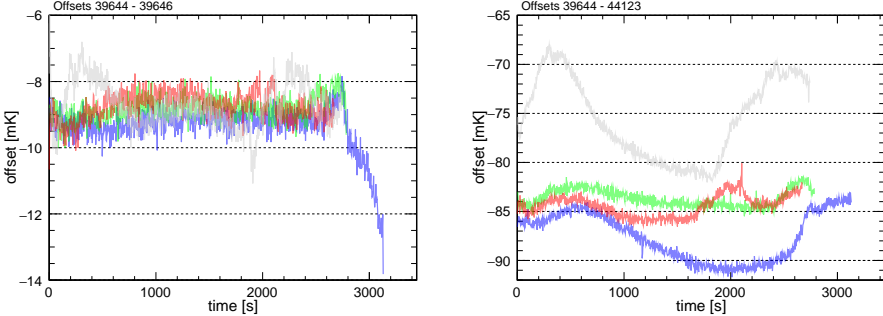


Figure 17: Left: The 4 measured offsets between two arbitrary sensors in the corona. Right: The 4 measured offsets between a sensor in the corona and one of the references, at the center.

436        The new calibration tree, shown in Fig. 18, contemplates four 12-sensors sets in the  
 437        first round, and a unique second round with three promoted sensors from each of the  
 438        sets in the first round. With this scheme, promoted sensors only suffer 8 baths, avoiding  
 439        the necessity of a time-walk correction.

440        The experimental procedure is similar to the one presented in Sec. 4. Two small  
 441        variations were introduced. First, the several concentric containers are cooled down  
 442        for 40 minutes before introducing the aluminium capsule for the first time in a day,  
 443        slightly improving the results of the first calibration run. Second, the warm up process  
 444        is accelerated using a heat gun, avoiding the use of water.

### 445        5.3. Calibration results

446        A sensor in the second round is chosen as reference, since this minimizes the number of  
 447        operations for non promoted sensors. On the other hand, since there are three promoted  
 448        sensors per set, there are also three ways of computing the offset with respect to the  
 449        reference for the nine non promoted sensors in a set. The calibration constant for those  
 450        sensors is computed as the weighted average of the three ‘paths’, while its uncertainty is  
 451        computed as the standard deviation of the three values. The absolute reference chosen  
 452        for the rest of the analysis is sensor 40525.

453        For each of the paths, the error on the offset can be computed by quadratically adding  
 454        the individual uncertainties on each of the terms contributing to that specific offset.  
 455        Then, the average path offset is computed as the weighted mean of the different paths  
 456        by considering the different path offsets errors that are involved. Finally, the uncertainty

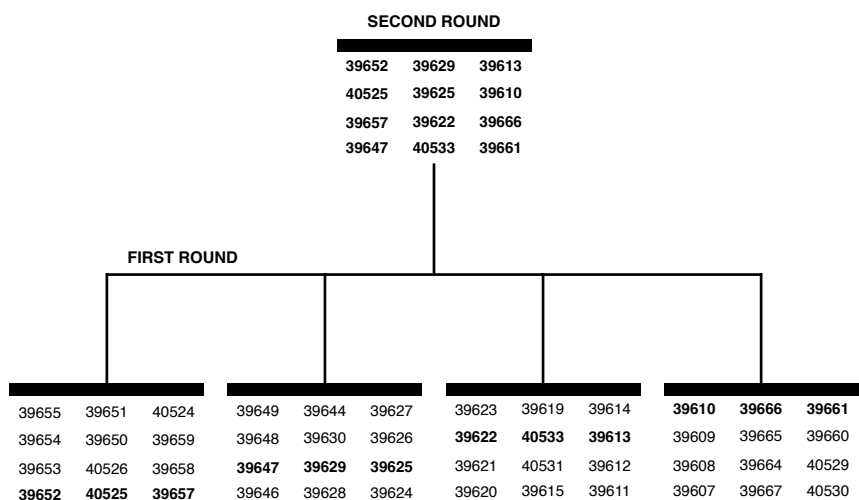


Figure 18: Schematic of the calibration strategy used with the new setup. Each of the sets contains 12 sensors, all of them placed in the corona, plus 2 references at the center. Sensors in bold in the first round are promoted to the second round.

457 on the average path offset is computed as the standard deviation of the involved path  
 458 offsets.

459 Fig. 19 shows the distribution of the repeatability (defined in Sec. 4.3.1) for the three  
 460 new calibrations mentioned in Table 1. In all three cases the error is slightly above 1  
 461 mK. Mean values are larger than the ones obtained in the 2018 calibration campaign.  
 462 This is attributed to the increased capsule size and the larger distance between sensors  
 463 inside the capsule. This hypothesis is supported by Fig. 20, showing the repeatability as  
 464 a function of the distance to the reference sensor in the corona for a particular measure-  
 465 ment. However, there is no substantial difference between the repeatability obtained for  
 466 LN2 and LAr calibrations.

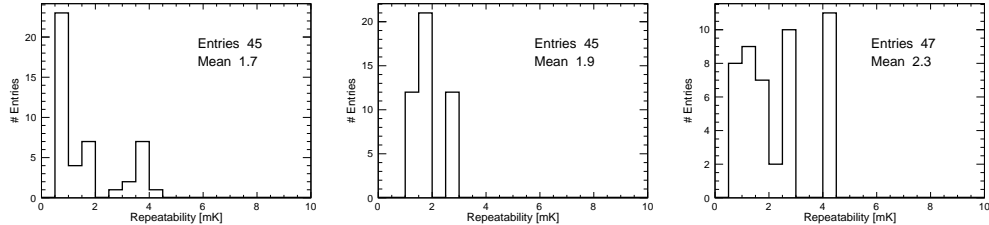


Figure 19: Repeatability distribution for the new calibrations. Left: LN2-2022. Middle: LN2-2023, Right:LAr-2023

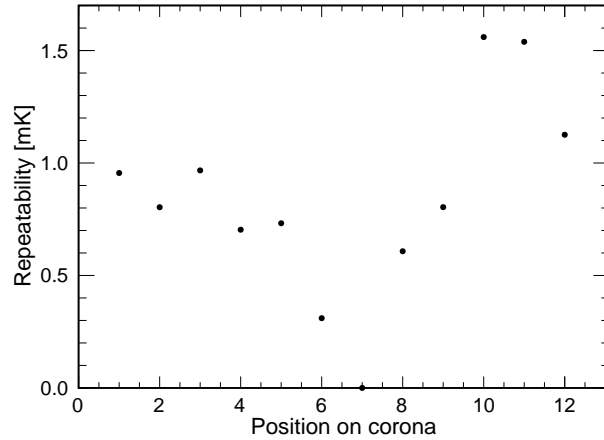


Figure 20: Repeatability as a function of position in the corona for the first set of the LAr-2023 calibration campaign.

467 Comparison between LN2 and LAr calibrations can also be used to understand the  
 468 dependence of the calibration constants on the absolute temperature. This is shown  
 469 in Fig. 21 along with other comparisons between calibration campaigns. The standard  
 470 deviation of the distribution is lower when comparing two calibrations in the same liquid  
 471 (LN2 in this case). However no bias is observed when comparing calibrations in two  
 472 different liquids, indicating that offsets are insensitive to a 10 K variation in absolute  
 473 temperature.

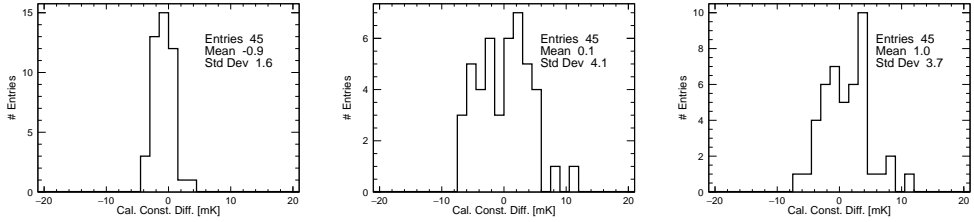


Figure 21: Difference between offsets for two calibrations. Left: LN2-2023 and LN2-2022. Middle: LAr-2023 and LN2-2022. Right: LAr-2023 and LN2-2023.

474 Ageing and long term stability have also been addressed. The left panel of Fig. 21  
 475 shows no difference between the offsets calculated in LN2 with a delay of one year. A bet-  
 476 ter understanding of this effect is achieved by comparing with the LAr-2018 calibration,  
 477 as shown in the next section.

#### 478 5.4. Comparison between new and old calibrations

479 Fig. 22 shows the distribution of the offset difference between the LAr-2018 and LAr-  
 480 2023 calibrations. The mean of the distribution is  $-0.1 \pm 0.6$  mK, excluding any relevant  
 481 systematic drift. The standard deviation of the distribution, 4.0 mK, is only slightly  
 482 larger than the ones obtained in the comparison between newer calibrations, which could  
 483 be due to the unknown contribution of the uncorrected readout offsets, pointing to small  
 484 or non-existing ageing effects. This can also be observed in Table 2, summarizing the  
 485 results of all possible comparisons between calibration campaigns, showing the mean and  
 486 standard deviation of those comparisons. The lowest standard deviation, 1.6 mK, is  
 487 obtained for the LN2-2022 to LN2-2023 combination, which is somehow expected since  
 488 i) the cryogenic liquid is the same, ii) ageing should be small since there is only one year  
 489 difference and iii) having use the same readout channels, readout offsets cancel out.

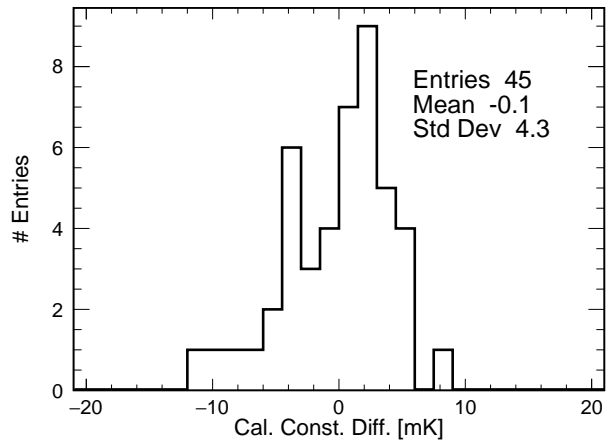


Figure 22: Difference between offsets for LAr-2018 and LAr-2023 calibration campaigns.

	LAr-2018	LN2-2022	LN2-2023	LAr-2023
LAr-2018	-	0.0, 3.5	0.9, 3.9	-0.1, 4.3
LN2-2022	-	-	0.9, 1.6	-0.1, 4.1
LN2-2023	-	-	-	-1.0, 3.7
LAr-2023	-	-	-	-

Table 2: Mean and standard deviation of the difference between the calibration constants obtained in two calibration campaigns.

490 The difference between the constants obtained in two calibration campaigns can be used  
491 to estimate the total calibration error. Since ProtoDUNE Horizontal Drift (ProtoDUNE-  
492 HD), the next iteration of the ProtoDUNE-SP detector, and DUNE will use LAr, the best  
493 estimation of the error would come from a LAr to LAr comparison close in time to the  
494 actual detector running. Being this combination not available, three other combinations  
495 can be used. The combination (LN2-2022)-(LN2-2023) has a standard deviation of 1.6  
496 mK, which should be the quadratic sum of the the errors of individual calibrations.  
497 Assuming this error is the same for both campaigns the single calibration error would be  
498 1.3 mK. In this comparison the readout channel offsets cancel out, but real fluctuations  
499 in those offsets contribute to the estimated single calibration error. Comparison between  
500 LAr-2018 and LAr-2023 also brings some insights into the single calibration error. The  
501 standard deviation is in this case 4.3 mK, corresponding to a single calibration error of  
502 3.0 mK. However, this value includes the uncorrected readout offsets as well as the effect  
503 of some potential ageing. Finally, comparison between LAr and LN2 calibrations in the  
504 new campaigns, avoids the readout offset and ageing problems, but suffer from potential  
505 dependence on the cryogenic liquid. Those comparisons have similar standard deviation  
506 of the order of 3.8 mK, corresponding to a single calibration error of 2.7 mK. This figure  
507 establishes an upper limit on the LAr calibration error. One can safely conclude that the  
508 individual calibration error in LAr is in the range 1.6-3.0 mK. This value is consistent  
509 with the one obtained using a different method for the LAr-2018 calibration, 2.4 mK (see  
510 Sec. 4.3.5).

## 511 6. Conclusions

512 The DUNE experiment will require the construction and operation of the largest cryostats  
513 ever used in a particle physics experiment. This makes the continuous measurement of  
514 temperature gradients in liquid argon crucial for monitoring the stability of the cryogenics  
515 system and for detector calibration. R&D on the calibration of RTD probes started in  
516 2017, leading to promising results for sensors installed in the DUNE prototype at CERN.

517 The first setup proved the viability of the method, obtaining a calibration error of 2.4  
518 mK. A key component was the readout electronics, with an intrinsic resolution better  
519 than 0.5 mK in the comparison between two channels. The mechanics was also crucial,

520 with several insulation layers consisting of independent concentric volumes, ensuring  
521 minimal convection in the inner volume. Sensors were contained in an aluminium capsule,  
522 enabling slow cool-down and warm-up processes, found to be fundamental to guarantee  
523 the integrity of the sensors and to minimize the effect of ageing.

524 The calibration system was later enhanced to accommodate the large-scale calibration  
525 required for the DUNE detectors. The capacity of the inner capsule was increased from  
526 4 to 14 sensors, while improvements were made to the insulation and symmetry of the  
527 system to minimize temperature differences between sensors. The new system has slightly  
528 worst repeatability for sensors in the same set, but reduces the statistical and systematic  
529 errors associated to the calibration tree, needed to relate any two sensors in different  
530 calibration sets. Calibration with the new setup has achieved a precision in the range of  
531 1.6-3.0 mK, substantially better than the 5 mK DUNE requirement.

532 Another difference between the new and old calibrations is the use of a different  
533 cryogenic liquid. While DUNE will use LAr, LN<sub>2</sub> is cheaper and more accessible in  
534 Spain, simplifying the process of massive calibration for DUNE detectors. The 10 K  
535 difference between those liquids has a minimal effect on the calibration constants.

536 A comparison of the four calibration campaigns has provided valuable insights into  
537 aging effects, with no evidence of RTD aging observed over a five-year period. This  
538 highlights the stability and reliability of the PT-102-based system.

## 539 7. Acknowledgments

540 The present research has been supported and partially funded by Conselleria d’Innovació,  
541 Universitats, Ciència i Societat Digital, by the Fundación ‘La Caixa’, and by MICINN.  
542 The authors would also like to thank all the people involved in the installation,  
543 commissioning and operation of ProtoDUNE-SP, specially to Stephen Ponders.

## 544 References

- 545 [1] Abi, B., et al. (DUNE), 2017. The Single-Phase ProtoDUNE Technical Design Report  
546 [arXiv:1706.07081](https://arxiv.org/abs/1706.07081).
- 547 [2] Abi, B., et al. (DUNE), 2020a. Deep Underground Neutrino Experiment (DUNE), Far Detector  
548 Technical Design Report, Volume I Introduction to DUNE. JINST 15, T08008. doi:10.1088/  
549 1748-0221/15/08/T08008, [arXiv:2002.02967](https://arxiv.org/abs/2002.02967).
- 550 [3] Abi, B., et al. (DUNE), 2020b. Deep Underground Neutrino Experiment (DUNE), Far Detector  
551 Technical Design Report, Volume II: DUNE Physics [arXiv:2002.03005](https://arxiv.org/abs/2002.03005).

- 552 [4] Abi, B., et al. (DUNE), 2020c. Deep Underground Neutrino Experiment (DUNE), Far Detector  
 553 Technical Design Report, Volume IV: Far Detector Single-phase Technology. JINST 15, T08010.  
 554 doi:10.1088/1748-0221/15/08/T08010, arXiv:2002.03010.
- 555 [5] Abi, B., et al. (DUNE), 2020d. First results on ProtoDUNE-SP liquid argon time projection  
 556 chamber performance from a beam test at the CERN Neutrino Platform. JINST 15, P12004.  
 557 doi:10.1088/1748-0221/15/12/P12004, arXiv:2007.06722.
- 558 [6] Abi, B., et al. (DUNE), 2020e. Long-baseline neutrino oscillation physics potential of the DUNE  
 559 experiment. Eur. Phys. J. C 80, 978. doi:10.1140/epjc/s10052-020-08456-z, arXiv:2006.16043.
- 560 [7] Abi, B., et al. (DUNE), 2021a. Prospects for beyond the Standard Model physics searches  
 561 at the Deep Underground Neutrino Experiment. Eur. Phys. J. C 81, 322. doi:10.1140/epjc/  
 562 s10052-021-09007-w, arXiv:2008.12769.
- 563 [8] Abi, B., et al. (DUNE), 2021b. Supernova neutrino burst detection with the Deep Under-  
 564 ground Neutrino Experiment. Eur. Phys. J. C 81, 423. doi:10.1140/epjc/s10052-021-09166-w,  
 565 arXiv:2008.06647.
- 566 [9] Abud, A.A., et al. (DUNE), 2022. Design, construction and operation of the ProtoDUNE-SP Liquid  
 567 Argon TPC. JINST 17, P01005. doi:10.1088/1748-0221/17/01/P01005, arXiv:2108.01902.
- 568 [10] Acciarri, R., et al. (MicroBooNE), 2017. Design and Construction of the MicroBooNE Detector.  
 569 JINST 12, P02017. doi:10.1088/1748-0221/12/02/P02017, arXiv:1612.05824.
- 570 [11] Adamowski, M., et al., 2014. The Liquid Argon Purity Demonstrator. JINST 9, P07005. doi:10.  
 571 1088/1748-0221/9/07/P07005, arXiv:1403.7236.
- 572 [12] Adams, D.L., et al., 2020. Design and performance of a 35-ton liquid argon time projection chamber  
 573 as a prototype for future very large detectors. JINST 15, P03035. doi:10.1088/1748-0221/15/03/  
 574 P03035, arXiv:1912.08739.
- 575 [13] Amerio, S., et al. (ICARUS), 2004. Design, construction and tests of the ICARUS T600 detector.  
 576 Nucl. Instrum. Meth. A 527, 329–410. doi:10.1016/j.nima.2004.02.044.
- 577 [14] Axon, . Axon custom cables. URL: [https://www.axon-cable.com/en/00\\_home/00\\_start/00/index.aspx](https://www.axon-cable.com/en/00_home/00_start/00/index.aspx). last visited: 2022-10-01.
- 578 [15] application bulletin, B.B., . Implementation and applications of current sources and current re-  
 579 ceivers. URL: <https://www.ti.com/lit/an/sboa046/sboa046.pdf?ts=1712062207089>. last visited:  
 580 2024-04-02.
- 581 [16] Chojnacki, E., 2009. A Multiplexed RTD Temperature Map System for Multi-Cell SRF Cavities,  
 582 in: SRF2009, p. 232.
- 583 [17] García-Peris, M.A., 2018. ProtoDUNE T-Gradient development and calibration. Master's thesis.  
 584 Valencia U. doi:10.2172/1780813.
- 585 [18] Hahn, A., Adamowski, M., Montanari, D., Norris, B., Reichenbacher, J., Rucinski, R., Stewart,  
 586 J., Tope, T. (LBNE), 2016. The LBNE 35 Ton Prototype Cryostat, in: 2014 IEEE Nuclear Sci-  
 587 ence Symposium and Medical Imaging Conference and 21st Symposium on Room-Temperature  
 588 Semiconductor X-ray and Gamma-ray Detectors. doi:10.1109/NSSMIC.2014.7431158.
- 589 [19] Instruments, N., a. Compactrio systems. URL: <https://www.ni.com/es/shop/compactrio.html>. last  
 590 visited: 2024-04-02.
- 591 [20] Instruments, N., b. Ni-9238. URL: <https://www.ni.com/es-es/shop/model/ni-9238.html>. last  
 592 visited: 2024-04-02.
- 593 [21] LakeShore, . Platinum sensors applications. URL: <https://www.lakeshore.com/products/categories/overview/temperature-products/cryogenic-temperature-sensors/platinum>. last  
 594 visited: 2023-05-18.
- 595 [22] Minco, . Resistance thermometry. URL: <https://www.minco.com/wp-content/uploads/Resistance-Thermometry.pdf>. last visited: 2023-05-18.
- 596 [23] Tektronix, . Keithley 2001 digit high performance multimeter. URL: [https://download.tek.com/datasheet/1KW-73954-1\\_2001-2002\\_DMM\\_Datasheet\\_080323.pdf](https://download.tek.com/datasheet/1KW-73954-1_2001-2002_DMM_Datasheet_080323.pdf). last visited: 2024-04-02.
- 597 [24] TempSens, . Rtd cables. URL: <https://tempsens.com/catalog/cables-wires/rtd-triad-cables.html>. last visited: 2024-03-15.
- 598 [25] Xiao, Y. (DUNE), 2021. Purity monitoring for ProtoDUNE-SP. J. Phys. Conf. Ser. 2156, 012211.  
 599 doi:10.1088/1742-6596/2156/1/012211.